Research Square

Preprints are preliminary reports that have not undergone peer review.
They should not be considered conclusive, used to inform clinical practice,
or referenced by the media as validated information.

Octopus-Inspired Implants for Rapid Deployment and Active Localization of Biochemical Abnormalities

Jing Zhao

jingzhao@bit.edu.cn

Beijing Institute of Technology https://orcid.org/0000-0002-0786-785X

Zhongyi Li

Beijing Institute of Technology

Lifeng Wu

Beijing Institute of Technology

Yiqi Yin

Beijing Institute of Technology

Zhejian Feng

Beijing Institute of Technology

Guozhen Shen

Beijing Institute of Technology https://orcid.org/0000-0002-9755-1647

La Li

Beijing Institute of Technology https://orcid.org/0000-0001-7355-0407

Article

Keywords:

Posted Date: November 19th, 2026

DOI: https://doi.org/10.21203/rs.3.rs-11691299/v1

License: This work is licensed under a Creative Commons Attribution 4.0 International License.
Read Full License

Additional Declarations: There is **NO** Competing Interest.

Octopus-Inspired Implants for Rapid Deployment and Active Localization of Biochemical Abnormalities

Zhongyi Li[1,2#], Lifeng Wu[3#], Yiqi Yin[1,2#], Zhejian Feng[1,2], Guozhen Shen[3*], La Li[3*], Jing Zhao[1,2,*]

[1]Key Laboratory of Biomimetic Robots and Systems (Beijing Institute of Technology), Ministry of Education, Beijing 100081, China

[2]School of Mechatronical Engineering, Beijing Institute of Technology, Beijing 100081, China

[3]School of Integrated Circuits and Electronics, Beijing Institute of Technology, Beijing 100081, China.

[#]These authors contributed equally

*Corresponding author Email: gzshen@bit.edu.cn, lali@bit.edu.cn, jingzhao@bit.edu.cn.

Abstract

Timely identification of localized biochemical abnormalities within internal organs remains challenging, as conventional diagnostic approaches often involve multistep procedures, while implantable sensors are typically restricted to predetermined monitoring sites. Here, we present an octopus-inspired, battery-free implantable sensing platform, termed the Tentacle Wireless Sensor (TWS), that integrates rapid minimally invasive deployment, high-performance wireless electrochemical sensing, and active biochemical exploration. By coupling an ultrathin, magnetically navigable electrochemical interface to a spatially separated wireless resonant module, TWS minimizes the dimensions of the deep-tissue sensing probe while preserving wireless readout functionality. The flexible interface can be deployed through a miniature puncture-based access route within 87 s, enabling immediate wireless biochemical interrogation without additional subcutaneous implantation. The system achieves a stationary pH resolution of 0.1 units and a complete response within 0.609 s to a large pH transition. We demonstrate magnetically guided navigation and spatially distributed electrochemical sensing in abdominal and intracranial environments, including active localization of leakage-associated pH abnormalities and oxidation-potential sensing. This platform establishes a strategy for rapidly deployable, spatially adaptive implantable bioelectronics, offering opportunities for timely localization and on-demand assessment of biochemical abnormalities.

Introduction

Timely identification of biochemical abnormalities within internal organs is critical for effective clinical intervention, particularly when localized pathological changes can rapidly progress into severe complications[1]. Conventional diagnostic approaches, including medical imaging and laboratory analyses, provide essential clinical

information but often involve multistep workflows that can require tens of minutes to several hours[2]. For instance, postoperative gastrointestinal leakage is commonly assessed using computed tomography (CT), inflammatory biomarkers, and drainage-fluid analyses, yet early or subtle leakage may remain difficult to identify before definitive radiological or systemic manifestations emerge[3,4]. Similarly, intracranial inflammation is evaluated through cerebrospinal fluid (CSF) analysis, supplemented by neuroimaging when clinically indicated, but these approaches do not readily provide continuous, spatially resolved information about local biochemical microenvironments [5]. Moreover, the location of early biochemical abnormalities may be uncertain, and their spatial distribution and evolution can be difficult to characterize through intermittent examinations. These limitations highlight the need for complementary technologies capable of rapidly accessing internal physiological environments and providing sensitive, spatially resolved biochemical information on demand.

Recent advances in implantable bioelectronics have enabled wireless biochemical monitoring and minimally invasive access to internal physiological environments[6–13]. Bioresorbable wireless pH sensors and injectable ultrasound-responsive materials have demonstrated promising approaches for monitoring gastrointestinal leakage, but their spatial coverage is largely determined by the initial placement of sensing elements, while hydrogel-mediated transduction can limit response speed[14,15]. In parallel, movable bioelectronic interfaces, including NeuroWorm and endocisternal neural interfaces, have enabled navigation and dynamic repositioning within internal tissues [16,17]. Despite their miniaturized sensing interfaces, these systems primarily focus on electrophysiological or biomechanical functions and still require associated signal-acquisition electronics and interconnections. Magnetically controlled self-sensing microrobots have further demonstrated wireless environmental monitoring, although

their sensing mechanisms predominantly rely on changes in surrounding electromagnetic properties rather than direct electrochemical interrogation of local biochemical signals[18–20]. Thus, existing approaches have advanced either wireless biochemical monitoring or actively repositionable sensing interfaces, but integrating rapid minimally invasive deployment, immediate wireless electrochemical interrogation, and active localization of abnormalities at initially unknown positions remains challenging (SI Appendix, Table S1).

At the device level, achieving these capabilities requires reconciling competing demands on implantation dimensions, mechanical compliance, and electronic functionality. Minimally invasive access to deep and confined anatomical spaces favors ultrathin, compliant sensing interfaces, whereas reliable wireless electrochemical measurements require electronic transduction and signal readout[21–25]. Incorporating these functions into a movable sensing structure can increase its dimensions and mechanical constraints, potentially compromising accessibility and navigation[26,27]. Geometrically reconfigurable bioelectronic implants have demonstrated that insertion dimensions can be reduced while retaining wireless functionality after deployment [28,29]. Nevertheless, enabling a deeply implanted sensing interface to independently navigate multiple anatomical locations while maintaining precise electrochemical measurements presents a distinct challenge. Balancing the dimensions of the tissue-interfacing components with the electronic functionality required for active biochemical exploration therefore remains an important consideration in the design of implantable bioelectronics[30].

Here, we report an octopus-inspired, battery-free implantable sensing platform, termed the Tentacle Wireless Sensor (TWS), that integrates an ultrathin, magnetically navigable electrochemical interface with a spatially separated wireless resonant module.

Inspired by the compliant and exploratory characteristics of octopus tentacles, this architecture decouples the deep-tissue sensing interface from the electronic module, enabling minimally invasive access and active exploration without introducing the entire electronic assembly into the target anatomical space. In a representative abdominal procedure, the sensing interface was deployed within 87 s, after which wireless biochemical interrogation could commence without additional subcutaneous implantation. Optional subcutaneous placement of the resonant module further enables a fully implanted configuration. The system achieves a stationary pH resolution of 0.1 units and a complete response within 0.609 s to a pH transition from 7.2 to below 2.2. We further demonstrate magnetically guided navigation and spatially distributed electrochemical sensing in abdominal and intracranial environments, including active localization of leakage-associated pH abnormalities and oxidation-potential (OP) sensing. By combining rapid deployment, high-performance wireless electrochemical sensing, and active spatial exploration, TWS provides a strategy for timely localization and on-demand assessment of biochemical abnormalities within internal anatomical environments.

Results

Working principle of the TWS

The design of the TWS draws inspiration from the ability of octopuses to use slender and highly dexterous arms to access confined spaces, explore their surroundings and maintain stable contact with local targets while remaining connected to a larger central body (Fig. 1A). Translating this functional organization into an implantable sensing platform, the TWS separates the relatively large wireless unit from a thin, flexible and mobile distal sensing interface (Fig. 1B). The wireless transceiver can remain extracorporeal or be implanted subcutaneously, whereas the tentacle-like

electrode can be introduced through a small access opening and magnetically guided within confined anatomical spaces. A magnetic element integrated at the distal end enables remote navigation, repositioning and fixation. The distal tip incorporates a modular electrochemical sensing interface that converts local physiological parameters into electrical potentials, allowing different voltage-based sensing modalities, including pH sensing and oxidation potential (OP) sensing.

The proximal wireless unit uses a passive LCR resonant architecture and is interrogated through near-field inductive coupling with an external reader, eliminating the need for an integrated battery. Changes in the electrochemical potential at the distal sensing interface modulate the resonant circuit and are encoded as shifts in resonance frequency. Physical and electrical decoupling between the mobile electrode and the stationary wireless unit minimizes motion-induced perturbations of the readout while preserving the ability of the sensing interface to move independently. As illustrated in Fig. 1C, the TWS can therefore be navigated under image guidance to scan previously uncharacterized regions, sequentially interrogate multiple anatomical sites and, once a region of interest is identified, remain at that location for continuous monitoring. This explores–localize–monitor mode forms the basis for spatially adaptive physiological sensing with the TWS.

Physically decoupled wireless sensing architecture of the TWS

The TWS employs a passive LCR architecture to minimize the number of electronic components and eliminate the requirement for an on-board power source, thereby reducing the footprint and implantation burden of the subcutaneous transceiver. As illustrated in Fig. 2A, voltage sensing is implemented using a varactor-based tunable resonant circuit. The low-frequency sensing pathway is electrically isolated from the radiofrequency (RF) resonator through a series decoupling resistor, while the distal

sensing electrode modulates the reverse-bias voltage applied to the varactor. Local physiological signals are converted into electrical potentials by a sensing interface comprising a functionalized working electrode and a custom reference electrode, and the resulting voltage changes the varactor capacitance and, consequently, the resonance frequency of the LCR circuit. The resonance is interrogated wirelessly through near-field inductive coupling with an external reader (31, 32). The distal sensing interface is fabricated from a flexible PI/Au electrode with a total thickness of approximately 30 μm to minimize mechanical loading on surrounding tissues (33, 34). The working electrode is integrated with a magnetic needle for remotely controlled navigation. Because the reverse-bias resistance of the varactor exceeds 100 MΩ, the sensing input can be approximated as an open circuit under quasi-static conditions, minimizing the influence of motion-induced changes in interconnect impedance on the measured sensing potential.

The voltage-to-frequency transduction characteristics of the wireless resonator are shown in Fig. 2B. Increasing the applied bias voltage resulted in a progressive shift of the resonance towards higher frequencies, yielding an approximately linear voltage–frequency relationship (Fig. 2C) with a sensitivity of approximately 0.04 MHz/mV. We next investigated whether spatial misalignment between the external reader and the TWS transceiver affected the recovered sensing signal. Reflection spectra were recorded while varying the relative lateral position of the two coils in the x–y plane and their vertical separation (Fig. 2D, E). At a vertical separation of 5 mm, the resonance amplitude progressively decreased from the center towards the periphery of the interrogation region as the mutual inductive coupling weakened (Fig. 2F). Despite this pronounced amplitude variation, the resonance frequency remained readily identifiable throughout the sensing region. Conversion of the position-dependent frequency shifts

into equivalent input voltages resulted in an error of only approximately 4 mV, even at peripheral positions with substantially reduced coupling (Fig. 2G). Similarly, the extracted resonance frequency remained nearly unchanged as the vertical separation increased from 4 to 12 mm (Fig. 2H). The frequency-encoded sensing mechanism is substantially less sensitive to variations in reader–transceiver coupling than signal amplitude reading, thereby enabling stable wireless interrogation under spatial misalignment.

We further examined whether motion of the distal sensing electrode could perturb the wireless resonance through changes in the parasitic impedance of the flexible interconnect. The electrode inductance was measured at different bending configurations (Fig. 2I, J) and varied from approximately 120 to 240 nH as the included angle changed from 0° to 180°. Continuous measurements during electrode motion showed a comparable inductance range (Supplementary Fig. 2). To determine an appropriate decoupling resistance, the self-inductances and mutual coupling of the reader and transceiver coils were first extracted using three-dimensional electromagnetic simulations and subsequently incorporated into an equivalent circuit model in Advanced Design System (ADS). A parasitic capacitance of 100 pF was introduced to represent a deliberately large parasitic load. At low decoupling resistance, variations in parasitic inductance produced pronounced shifts in the resonance frequency; this dependence progressively decreased with increasing resistance and became negligible at 10 kΩ (Supplementary Fig. 3 and Fig. 2K). A 10-kΩ series resistor was therefore used in all subsequent experiments to electrically decouple motion of the distal sensing interface from the RF resonator. This physically and electrically decoupled architecture allows the distal electrode to be actively repositioned while the stationary transceiver maintains a stable frequency-encoded wireless readout.

This spatially decoupled architecture enables the electrochemical sensing interface to be independently optimized for minimally invasive implantation and active navigation, while the wireless resonant module provides electronic transduction without imposing additional size constraints on the deep-tissue probe. The ultrathin, compliant interface can therefore access confined anatomical environments through miniature openings while retaining high-performance wireless biochemical sensing. Moreover, separating the sensing interface from the electronic module allows flexible deployment configurations, including optional subcutaneous placement of the resonant module for fully implanted operation. This design enables active interrogation of multiple locations through a single deep-tissue access route, without requiring repeated implantation or repositioning of the entire electronic assembly.

Magnetic navigation and actuation characteristics of the TWS

To evaluate the navigation capability of the TWS in a tissue-mimicking environment, we used 0.6 wt% agar to reproduce the compliant mechanical environment encountered in soft biological tissues. As shown in Fig. 3A, the TWS entered the agar from one side and was subsequently advanced and steered under an externally applied magnetic field. The device followed an S-shaped scanning trajectory before returning to a position close to the initial entry site, demonstrating controllable forward motion and directional steering within the confined gel environment.

We next quantified the magnetic actuation conditions required to drive the TWS. The TWS was embedded in the agar while a spherical permanent magnet was progressively moved towards the distal magnetic needle (Fig. 3B, C). As the separation decreased, the magnetic needle transitioned from negligible displacement to gradual motion and finally to rapid translation (Supplementary Video 1). The corresponding needle displacement and magnet–needle separation are plotted in Fig. 3D. Three

pronounced transitions in the displacement response were observed. To identify these transition points more clearly, we calculated the derivative of needle displacement with respect to magnet–needle separation (right axis, Fig. 3D), revealing characteristic distances of 16.57, 14.08 and 8.93 mm. In particular, once the separation reached approximately 8.93 mm, the TWS entered a regime of sustained rapid motion, providing a practical operating distance for robust magnetic actuation.

To determine the magnetic conditions associated with these transitions, we established a finite-element model in COMSOL Multiphysics (Fig. 3E). The experimentally measured magnetic flux density as a function of distance agreed well with simulations using a remanent flux density of 0.8 T (Fig. 3F). The inset shows the simulated field distribution at a separation of 10 mm, with the magnetic flux density decreasing progressively away from the center of the spherical magnet. Because the translational force acting on the magnetic tip is governed by the spatial gradient of the magnetic field, we further extracted the magnetic-field gradient as a function of distance for magnets with different remanent flux densities (Fig. 3G). The field gradient decreased rapidly with increasing separation. Using the 0.8 T model as the experimentally validated reference, the three characteristic transition conditions identified in Fig. 3D were mapped onto the corresponding actuation distances for magnets with different remanent flux densities. Increasing the remanent flux density extended the effective actuation distance to beyond 20 mm, indicating that the magnetic driving range can be adjusted to accommodate different anatomical depths. For routine operation, we used the shortest characteristic actuation distance to provide rapid and reliable locomotion. Longer-range actuation can be achieved by increasing the magnetic strength or volume of the external NdFeB magnet, whereas increasing the size of the distal magnetic needle provides an additional means of enhancing the available

magnetic force (Supplementary Fig. 4 and Supplementary Note3).

Physiological sensing performance

The TWS converts the direct-current potential generated at the distal sensing interface into a frequency-encoded radiofrequency signal, allowing the same wireless architecture to accommodate different electrochemical sensing modalities. To demonstrate this versatility in abdominal and intracranial applications, we evaluated the TWS using pH and OP sensing, respectively. In the abdominal cavity, leakage from organs such as the stomach, pancreas and small intestine can lead to severe complications, including intra-abdominal infection, and local pH changes may provide an early indication of leakage before systemic deterioration occurs. For intracranial applications, OP provides a complementary electrochemical signal that can reflect changes in the local inflammatory microenvironment.

For pH sensing, a polyaniline (PANI)-modified Au electrode was used as the working electrode, together with a custom Ag/AgCl reference electrode coated with a KCl–poly(vinyl butyral) (PVB) membrane. Representative wireless spectra obtained at different pH values are shown in Fig. 4A. The TWS exhibited a pronounced frequency response over a broad pH range from pH 8 to pH 4, with the resonance progressively shifting towards higher frequencies as the pH decreased. Repeated stepwise cycling further demonstrated stable and reproducible responses at each pH level (Fig. 4B). The corresponding calibration curve yielded a sensitivity of 2.32 MHz/pH (Fig. 4C). To determine whether movement of the distal pH electrode affected voltage transfer to the wireless transceiver, we measured the electrode impedance under different spatial configurations (Fig. 4D). The impedance remained below 20 kΩ, substantially smaller than the effective input resistance of the RF sensing circuit, indicating that motion-induced impedance variations contributed negligibly to the transmitted sensing

potential.

The OP-sensing TWS exhibited a similarly monotonic frequency response to changes in electrode potential (Fig. 4E). Increasing OP shifted the resonance towards higher frequencies, while repeated measurements at each potential showed stable responses. The resulting voltage-to-frequency sensitivity was approximately 0.045 MHz/mV. As with the pH electrode, variations in electrode impedance caused by repositioning remained much smaller than the input resistance of the wireless circuit and therefore had little effect on signal transduction. The custom reference electrode also showed minimal potential variation during repeated pH cycling from pH 8 to pH 4 (Supplementary Fig. 6), with fluctuations substantially smaller than the pH-dependent response of the sensing electrode.

We further evaluated the resolution and dynamic response of the pH-sensing TWS. As shown in Supplementary Fig. 7, the system reliably distinguished a pH change from 7.0 to 6.9, corresponding to a resolution of 0.1 pH unit. The sensor also responded rapidly to an abrupt large-amplitude pH change, with a measured response time of 0.609 s. Combined with stable wireless readout during distal-interface repositioning, these characteristics enable the TWS to perform high-resolution and rapid electrochemical sensing during active navigation.

Active physiological mapping by the TWS

To evaluate the capability of the TWS for active environmental sensing, we first performed spatial mapping in a homogeneous pH environment (Supplementary Fig. 8 and Supplementary Video 2). The reference electrode was immersed in the same solution but positioned outside the imaging field, and a colorimetric pH indicator was added to visualize the spatial distribution of pH. The TWS was magnetically guided along an S-shaped scanning trajectory while its position and resonance frequency were

recorded simultaneously. Throughout the scan, the resonance-frequency variation was limited to approximately 0.3 MHz, corresponding to a pH variation of only ~0.13, demonstrating stable sensing during active navigation in a homogeneous environment.

We next introduced dilute sulfuric acid on one side of the chamber to generate a localized acidic region (Fig. 4I and Supplementary Video 3). Although movement of the TWS induced gradual mixing and redistribution of the pH gradient, the sensor continuously tracked the local pH encountered along its trajectory (Fig. 4J), enabling reconstruction of the evolving spatial pH distribution. To further evaluate sensing in a geometrically complex environment, we fabricated a three-dimensional vessel-network model by 3D printing (Supplementary Fig. 9A). A localized acidic region was generated at one side of the network, and the TWS was guided along a predefined trajectory while pH and device position were recorded simultaneously. The spatial pH map reconstructed from the measured pH values and visually tracked TWS coordinates is shown in Supplementary Fig. 9B. Regions represented by warmer colors corresponded to lower pH values, and the reconstructed distribution closely matched that visualized by the colorimetric indicator, demonstrating that the TWS can combine active navigation with spatially resolved physiological sensing in confined and branched environments.

We further constructed a three-dimensional cranial model to evaluate active sensing within an anatomically relevant environment. A localized acidic region was generated in the anterior portion of the cranial cavity by introducing dilute sulfuric acid through a catheter. The TWS was introduced through a predefined cranial access port and actively navigated using an external spherical magnet. Starting from a region with baseline pH, the TWS was guided towards the central and peripheral regions of the localized pH abnormality, and the same navigation sequence was repeated twice (Fig.

4K). The corresponding wireless responses are shown in Fig. 4L. Lower pH values were detected within the central region of the acidic zone, whereas higher pH values were measured near its periphery. The frequency-shift profiles obtained during the two repeated scans were highly consistent, demonstrating the ability of the TWS to repeatedly interrogate distinct locations within the same three-dimensional space and reproducibly resolve spatial variations in the local physiological environment.

Minimally invasive implantation and in vivo navigation of the TWS

The functionalized TWS can be introduced into the body through pre-established micro-access channels to perform sensing and exploratory tasks. The overall implantation procedure is illustrated in Fig. 5A and Supplementary Video 6. A minimally invasive access route was first established with a diameter only slightly larger than that of the TWS head. For intracranial applications, this access route can be created using a microdrill. For abdominal implantation, however, the compliant abdominal wall tends to deform and collapse, making direct insertion difficult; a puncture-assisted approach was therefore used to establish the implantation channel. To facilitate visualization, a transparent catheter was used as a temporary access conduit. Specifically, the catheter was advanced into the abdominal cavity over a puncture needle, after which the needle was withdrawn to leave a temporary implantation channel. The flexible distal electrode was then introduced through the catheter into the abdominal cavity. Because of its high compliance, the electrode was magnetically pulled forward during insertion. After implantation of the distal electrode, the catheter was removed. To enable rapid integration of the sensing electrode with the wireless transceiver, we adopted a magnet-based quick mechanical and electrical connection. Permanent magnets were attached to the reserved terminals of both the transceiver and the sensing electrode using conductive silver paste, so that simple proximity was

sufficient to achieve simultaneous electrical and mechanical coupling. The junction was subsequently insulated using a biocompatible adhesive. For long-term applications, the miniature transceiver can be implanted subcutaneously to avoid chronic percutaneous connections and reduce the associated risk of infection. Its small diameter and low thickness make it well suited for subcutaneous placement.

Establishing the catheter-based access route required 57 s, followed by 30 s for insertion of the flexible sensing probe, allowing the deep-tissue electrochemical interface to be deployed within 87 s. For applications requiring a fully implanted configuration, optional electrical connection and subcutaneous implantation of the wireless resonant module required an additional 111 and 264 s, respectively, resulting in a total recorded procedure time of 561 s (9 min and 21 s). Notably, the subcutaneous implantation step is optional rather than a prerequisite for deploying the deep-tissue sensing interface. Once positioned, the magnetically navigable probe can explore multiple anatomical locations through the same access route without repeated deep-tissue implantation. This modular deployment strategy combines rapid establishment of a minimally invasive sensing interface with the flexibility to select the wireless module configuration according to monitoring requirements.

We next characterized active in vivo navigation of the TWS. Abdominal navigation was first evaluated in rabbits, as shown in Fig. 5B and Supplementary Fig. 10. Anaesthetized rabbits were placed in a digital subtraction angiography (DSA) system, while the external actuation magnet was mounted on a motorized stage to enable remote navigation of the TWS. A reader coil was positioned on the body surface for wireless interrogation, and the system was controlled through a host computer. As shown in Supplementary Video 7, the magnetic tip of the TWS could be remotely translated and steered within the abdominal cavity under the guidance of the external

spherical magnet, allowing it to access multiple regions for interrogation. Resonance-frequency shifts recorded during motion remained below 0.06 MHz, indicating that locomotion introduced negligible interference into the wireless readout.

We further explored intracranial navigation of the TWS, as shown in Fig. 5C. The device was able to move within the subdural space while transmitting sensing signals in real time to an extracranial reader. We first established a visible cranial window by removing part of the skull (upper panel of Fig. 5D and Supplementary Video 8). The magnetic tip of the TWS was introduced into the subdural space through a small incision and guided forward by the external magnetic sphere. Although the subdural space in rabbits is considerably narrower than that in humans, the TWS was still able to perform controlled exploratory motion within this confined environment. To further validate minimally invasive intracranial deployment, a burr hole with a diameter of 1.2 mm was created in the skull of a second rabbit, and the TWS was inserted through this opening into the intracranial space. The device was then navigated under DSA guidance (lower panel of Fig. 5D and Supplementary Video 9). The ability to deploy and navigate the TWS through a millimeter-scale cranial access port, together with its abdominal navigation capability, supports minimally invasive active exploration and physiological sensing across distinct anatomical spaces. These results demonstrate that the electronics-enabled electrochemical interface can be rapidly introduced into deep anatomical environments through a minimally invasive access route and subsequently navigated across multiple locations, enabling spatially distributed biochemical sensing without repeated deep-tissue implantation.

Active in vivo sensing and biomedical validation of the TWS

The combination of active sensing and minimally invasive deployment enables the TWS to overcome a fundamental limitation of conventional implantable sensors, whose

fixed sensing locations largely restrict measurements to predefined anatomical sites. This spatial constraint limits the use of highly sensitive implantable sensors for detecting localized abnormalities whose positions are not known in advance. We first evaluated the TWS for monitoring local physiological states within the abdominal cavity. Leakage of luminal or glandular contents from abdominal organs can generate pronounced local changes in pH, providing a biochemical signature that can be detected directly at the affected site (Fig. 6A). Gastric leakage produced the largest pH change. Representative spectra acquired from the intact gastric surface and a gastric incision showed a pronounced shift of the resonance towards higher frequencies (Fig. 6B). Continuous measurements revealed a frequency shift of approximately 14 MHz, corresponding to a pH difference of approximately 6 units (Fig. 6C). Pancreatic injury similarly produced a measurable resonance shift of approximately 2 MHz, corresponding to a pH change of about 0.96 unit (Fig. 6D, E). The response associated with small-intestinal leakage was smaller, with a frequency shift of approximately 0.7 MHz, equivalent to a pH change of about 0.3 unit. Despite the markedly different magnitudes of these local changes, the TWS was able to interrogate multiple abdominal organs and resolve their distinct physiological states, demonstrating the potential of a repositionable sensing interface for spatially distributed intra-abdominal monitoring.

We next investigated whether active sensing could provide complementary biochemical information in the intracranial environment. Although magnetic resonance imaging (MRI) can localize intracranial lesions, similar imaging appearances may conceal distinct pathological microenvironments. Direct measurement of local oxidation potential (OP) offers a means to differentiate these electrochemical states beyond anatomical imaging alone (Fig. 6H and Supplementary Fig. 11). We therefore established two intracranial injury models with different severities, based on autologous

blood injection and photothrombotic injury. Both produced imaging-visible lesions, but differed in their local electrochemical characteristics. Using an OP-sensitive TWS, we interrogated normal tissue and the two lesion types. As shown in Fig. 6I, the normal region exhibited the highest OP, whereas the photothrombotic lesion showed the lowest value; the autologous-blood model produced a more moderate decrease. The larger reduction observed in the photothrombotic model may reflect greater perturbation of the local redox environment. Spatially resolved OP measurements therefore provide electrochemical contrast complementary to anatomical imaging, enabling the TWS to distinguish intracranial regions with different pathological states.

We further assessed the implantation burden and stability of the TWS for extended use. To compare minimally invasive puncture implantation with conventional surgical implantation, TWS electrodes were introduced into the abdominal cavity either through a percutaneous puncture or through a 1–2-cm surgical incision. After 7 d, abdominal-wall tissues surrounding the implantation sites were collected and analyzed by haematoxylin and eosin staining. Histological analysis showed substantially less tissue disruption and inflammatory response after puncture implantation than after surgical incision (Supplementary Fig. 12). The stability of the sensing and encapsulation interfaces was also evaluated under prolonged exposure to physiological solution. After 6 d of immersion in PBS, the pH electrode retained its ability to resolve changes from pH 8 to pH 4 without an obvious loss of response (Supplementary Fig. 13). The encapsulation remained electrically insulating after 12 d of immersion in PBS (Supplementary Fig. 14). Finally, thermal measurements during continuous wireless interrogation showed no appreciable temperature increase under conditions relevant to subcutaneous operation (Supplementary Fig. 15). The reduced implantation-associated tissue injury, together with the stability of the sensing, encapsulation and wireless

interfaces, supports minimally invasive and extended physiological monitoring with the TWS.

Conclusion

In summary, we developed an octopus-inspired, battery-free implantable sensing platform that integrates rapid minimally invasive deployment, high-performance wireless electrochemical sensing, and active localization of biochemical abnormalities. By electronically coupling an ultrathin, magnetically navigable electrochemical interface to a spatially separated wireless resonant module, TWS minimizes the dimensions of the deep-tissue sensing probe without requiring the entire electronic assembly to enter confined anatomical spaces. The flexible sensing interface can be deployed through a miniature puncture-based access route within 87 s, enabling immediate wireless biochemical interrogation, while optional subcutaneous implantation of the resonant module supports fully implanted operation. The system achieves a stationary pH resolution of 0.1 units and a complete response within 0.609 s to a large pH transition, with measurement stability evaluated under different movement and wireless coupling conditions. We further demonstrate minimally invasive implantation, magnetically guided navigation, and spatially distributed electrochemical sensing in abdominal and intracranial environments, including active localization of leakage-associated pH abnormalities and oxidation-potential measurements. The integration of different electrochemical sensing interfaces further highlights the functional adaptability of this architecture beyond pH monitoring alone. By combining rapid deployment, active spatial exploration, and precise wireless biochemical sensing, TWS provides a strategy for extending implantable bioelectronics beyond fixed-site monitoring toward timely localization and on-demand assessment of physiological abnormalities.

Methods

Fabrication of a physically decoupled sensing platform

The sensing platform was designed to physically decouple the requirements for stable wireless interrogation from those for distal electrode motion. The proximal wireless transceiver was fabricated using a two-layer flexible printed circuit board with a total thickness of 0.11 mm. Two oppositely oriented SMV1249-040LF varactor diodes and a 10-kΩ resistor were assembled by surface-mount technology. The resistor electrically decoupled the low-frequency sensing signal from the radiofrequency resonant circuit, thereby minimizing interference between the sensing and wireless readout pathways. The flexible distal sensing electrode was fabricated using a cut-and-laminate process. A 10-μm-thick polyimide film was metallized with 20 nm of Ti and 100 nm of Au, with Ti serving as the adhesion layer and Au providing a chemically stable conductive and sensing interface. The metallized film was temporarily laminated onto thermal-release tape and patterned into slender electrodes using a cutting plotter (CE7000-40). After cutting, the patterned electrodes were released from the thermal-release tape on a hot plate and subsequently transferred onto a 5-μm-thick polyimide substrate. The electrodes were then encapsulated with polyimide adhesive and cured under vacuum at 200 °C for 4 h. The two ends of the electrode were left exposed to form the distal sensing interface and the proximal electrical contact, respectively. The resulting flexible electrode had an overall thickness of approximately 30 μm, providing a mechanically compliant connection between the stationary wireless transceiver and the mobile sensing interface.

Assembly, integration and functionalization of the TWS

The flexible sensing electrode was electrically connected to the predefined contact pads of the wireless transceiver using conductive silver paste, after which the

transceiver was encapsulated with polydimethylsiloxane (PDMS) for electrical insulation. For in vivo implantation, a detachable connection was introduced between the transceiver and the flexible electrode to facilitate removal of the implantation catheter after placement of the distal sensing interface. A magnetic disk was attached to the electrical terminal of the transceiver using conductive silver paste and subsequently insulated with PDMS, while a second magnetic disk was similarly attached to the proximal contact of the flexible sensing electrode. After implantation of the sensing electrode, the two magnetic terminals were coupled to establish rapid mechanical attachment and electrical connection between the distal sensing interface and the subcutaneous transceiver. The assembled junction was subsequently sealed with Loctite 4305.

For magnetic navigation, a NdFeB magnetic needle was attached to the distal end of the sensing electrode using Loctite 4305. Two magnetic-needle geometries were used according to the anatomical application. For intracranial experiments, a needle with a diameter of 0.5 mm and a length of 5 mm was used, whereas a needle with a diameter of 1 mm and a length of 3 mm was used for abdominal experiments. The magnetic needles were commercially obtained through Alibaba and were fully coated with Loctite 4305 before use to electrically insulate the magnetic material from the surrounding environment.

The sensing electrodes were functionalized by modifying the exposed Au interface with the corresponding sensing materials. For OP sensing, the bare Au electrode was used directly as the sensing interface without additional surface modification. For pH sensing, polyaniline (PANI) was electrodeposited onto the Au working electrode by cyclic voltammetry in an aqueous solution containing 0.25 M aniline and 0.5 M H_2SO_4. The potential was swept from −0.1 to 1.0 V for ten cycles using an Ag/AgCl reference

electrode and a Pt sheet counter electrode, resulting in the formation of a PANI sensing film on the working electrode.

A solid-state Ag/AgCl reference electrode was prepared using a poly(vinyl butyral) (PVB)–KCl matrix. Fine KCl particles were first obtained by recrystallization. Briefly, 50 g of KCl was dissolved in 100 mL of water at 80 °C under stirring to prepare a saturated solution. The solution was subsequently cooled in an ice bath under continuous stirring to induce recrystallization. After sedimentation, the supernatant was removed and the resulting KCl particles were washed five times with ethanol and dried under reduced pressure to remove residual solvent. A PVB–KCl precursor solution was then prepared by dispersing 0.60 g of PVB and 0.51 g of recrystallized KCl in 8 mL of methanol. Ag/AgCl paste was applied to the exposed Au electrode and cured at 150 °C for 30 min, after which the PVB–KCl solution was drop-cast onto the Ag/AgCl layer to form the solid-state reference electrode. Before use, the PANI pH electrode and the solid-state reference electrode were conditioned for 4–6 h in 1× phosphate-buffered saline (PBS) and saturated KCl solution, respectively, to stabilize their electrochemical response.

Characterization of the physiological sensing performance of the TWS

To characterize the physiological sensing performance of the TWS, both pH and OP sensors were evaluated using repeated stepwise cycling tests. The pH value or OP potential was progressively varied across multiple levels, with each step maintained for 100 s. The final reflection spectrum acquired at each step was retained as the representative response spectrum. To evaluate pH sensitivity at physiologically relevant resolution, the sensor response was further characterized over a narrow pH interval from pH 7.0 to pH 6.9. The dynamic response of the pH sensor was assessed by rapidly introducing a large volume of dilute sulfuric acid into 1× phosphate-buffered saline

(PBS), producing an abrupt decrease in pH from 7.2 to below 2.2. The corresponding wireless response was recorded continuously to determine the sensor response time.

The performance of the solid-state reference electrode was evaluated separately by conducting repeated pH cycling tests from pH 8 to pH 4. During these measurements, the responses of the PANI pH electrode and the custom-fabricated reference electrode were recorded simultaneously to assess the stability and reproducibility of the reference potential over repeated pH variations.

Characterization of the TWS sensing range and motion interference

The wireless sensing range of the TWS was characterized using a motorized translation stage combined with a vector network analyzer (VNA). A 10-mm-diameter printed-circuit-board coil was used as the external readout coil, and the TWS transceiver without the flexible sensing electrode was used as the test device. The VNA output power was set to −10 dBm with an intermediate-frequency bandwidth of 1 kHz. The relative position between the readout coil and the TWS was varied with a step size of 1 mm in both the x–y plane and the z direction. At each position, the reflectance spectrum was recorded, and the resonance frequency and peak amplitude were extracted from the raw data using a custom Python program to construct the spatial wireless sensing map.

Motion-induced interference was characterized using a combination of electromagnetic simulation, impedance measurements and circuit-level modelling. The self-inductances and mutual coupling coefficients of the relevant coils were first extracted using Ansys Maxwell. To quantify inductance variations associated with deformation and motion of the flexible electrode interconnect, its inductance was measured using 6500B impedance analyzer. A 20-cm-long wire was used to represent the electrode interconnect, and its geometry was varied by changing the included angle

from 0° to 180° to emulate position changes induced by distal motion. Dynamic variations in inductance were further recorded during continuous motion. An equivalent circuit model of the TWS was subsequently established in Advanced Design System (ADS). A parasitic capacitance of 100 pF was introduced to represent a deliberately large parasitic load, and the decoupling resistance was systematically varied. The corresponding resonance frequencies of the wireless transceiver were extracted to evaluate the influence of electrode motion and parasitic coupling on the stability of the wireless readout.

Characterization of TWS locomotion and navigation

To mimic the mechanical environment encountered during in vivo navigation, a 0.6 wt% agar gel was prepared as an in vitro locomotion medium. A spherical NdFeB permanent magnet with a diameter of 25 mm was used for magnetic actuation and navigation of the TWS. The force–distance relationship between the external magnet and the magnetic needle was characterized using a force gauge mounted on a motorized translation stage. The spherical magnet was held stationary, while the magnetic needle was attached to the probe of the force gauge and displaced relative to the magnet to record the magnetic force as a function of separation distance.

To quantify the magnetic-field gradient required to initiate and sustain TWS motion in the agar medium, the spherical magnet was mounted on a translation stage and progressively moved towards the TWS embedded in the agar gel. TWS motion was recorded during magnet approach, and the displacement of the TWS together with the corresponding distance between the magnetic needle and the spherical magnet was extracted using a custom Python program. The magnetic-field gradient corresponding to each separation distance was then determined from the calibrated magnetic-field profile, enabling estimation of the actuation threshold required for TWS locomotion in

the tissue-mimicking environment.

The magnetic-field distribution generated by the spherical magnet was simulated using COMSOL Multiphysics. The remanent flux density of the NdFeB magnet was varied in the model to evaluate the magnetic-field and field-gradient distributions produced by magnets with different magnetic strengths. The simulated field profiles were experimentally validated by measuring the magnetic flux density at different distances from the spherical magnet using a gaussmeter. The corresponding magnetic-field gradients were calculated from the spatial variation in magnetic flux density and compared with the simulated results.

Active in vitro navigation and physiological mapping with the TWS

To evaluate the sensing and mapping performance of the TWS, an in vitro physiological mapping platform was constructed using phosphate-buffered saline (PBS, pH 7.2) as the background medium. A colorimetric indicator was added to visualize the spatial pH distribution, and localized acidic regions were generated by introducing dilute sulfuric acid at selected positions. To facilitate visual tracking during navigation, the distal magnetic needle was replaced with a NdFeB magnetic disk measuring 3 mm in diameter and 1 mm in thickness, allowing the position of the TWS to be recorded simultaneously with the spatial features of the surrounding environment. The sensing accuracy was first evaluated in a spatially homogeneous PBS environment. Dilute sulfuric acid was then introduced on one side of the culture dish to generate a localized pH gradient, and the TWS was remotely navigated across the dish to reconstruct the spatial pH distribution. A vessel-mimicking structure was subsequently fabricated by 3D printing, and a localized acidic region was similarly introduced on one side of the model. The TWS was remotely navigated through the confined structure while continuously recording the local pH, thereby evaluating its ability to perform

physiological sensing and mapping within geometrically constrained environments.

To further assess TWS operation in a three-dimensional anatomical environment, a customized cranial model was reconstructed from medical imaging data and fabricated to reproduce the relevant intracranial geometry. The model was filled with PBS containing a colorimetric indicator to visualize the spatial distribution of pH. Two regions with relatively high and low pH were established, and the TWS was magnetically navigated back and forth between these regions for two consecutive cycles. The simultaneously recorded sensor position and pH response were used to evaluate the repeatability of active physiological mapping in a three-dimensional anatomical environment.

Animal

Rabbit experiments in this study were performed in accordance with protocols approved by the permission of Beijing Yike Xinye Biotechnology Co., Ltd. (Approval No. BW-IACUC-2026-039). New Zealand white rabbits were obtained from Beijing Vital River Laboratory Animal Technology Co., Ltd.

Surgical procedure in rabbits

All animal experiments mentioned in the text were conducted under the permission of Beijing Yike Xinye Biotechnology Co., Ltd. (Approval No. BW-IACUC-2026-039), and then were in accordance with the regulations.

Eighteen 6-month-old male New Zealand white rabbits, weighing 2-3 kg and free of any pathologies, were utilized in the research. These rabbits were individually housed in cages, subjected to a 12-hour light/dark cycle at temperatures of 22–25 °C and humidity levels of 55–60%, and provided with unrestricted access to food and water. Eighteen healthy adult rabbits were divided into six groups: intracranial autologous blood clot stroke model group (n=3), intracranial laser-induced brain injury model

group (n=3), DSA cranial monitoring and evaluation group (n=3), DSA intraperitoneal monitoring and evaluation group (n=3), intra-abdominal visceral organ injury model group (n=3), and long-term in vivo monitoring group (n=3). For monitoring procedures, animals were maintained under 2% isoflurane inhalation anesthesia, whereas deep anesthesia for all model-inducing surgeries was achieved via intravenous co-administration of Telazol 50 (tiletamine–zolazepam, 20 mg/kg) and xylazine (3 mg /kg), with anesthetic depth validated by pedal and corneal reflex assessment and continuous physiological monitoring of heart rate, respiratory rate and rectal temperature (38.0 ± 0.5 °C).

Focal cerebral infarction modeling and MRI evaluation

A focal intracranial ischemic infarction model was established in New Zealand rabbits using autologous blood clot embolization. The cervical skin was depilated and disinfected with alternating povidone–iodine and 75% ethanol to create a sterile surgical field. A longitudinal micro-incision was made on the anterior neck, followed by blunt dissection of subcutaneous tissues to expose the common carotid artery. For thrombus preparation, venous blood was aseptically collected from the marginal ear vein and incubated in sterile EP tubes at room temperature for 20–30 min to allow complete coagulation. The formed autologous clot was gently triturated and resuspended in sterile saline to form a homogeneous embolic suspension.

Under stereotactic microscopic guidance, a flexible microcatheter was inserted through the common carotid artery and advanced to the intracranial segment of the internal carotid artery. The clot suspension was slowly injected into the distal cerebral circulation to induce targeted vascular occlusion and establish focal cerebral ischemia. After injection and brief stabilization, the microcatheter was withdrawn, and the carotid puncture site was checked for hemostasis. The cervical subcutaneous and cutaneous

layers were finally sutured in layers to restore tissue integrity.

Immediately after modeling, anesthetized rabbits were scanned on a 3.0 T preclinical MRI system for in vivo validation of ischemic lesions. Diffusion-weighted imaging (DWI) and T2-weighted imaging (T2WI) sequences were acquired to identify acute ischemic regions, characterize lesion morphology, and quantify infarct volume, confirming the success of model establishment.

Focal cerebral inflammatory lesion induction via orange laser irradiation in rabbits

The scalp over the calvaria was depilated and disinfected with alternating povidone–iodine and 75% ethanol. A midline scalp incision was made, and the periosteum was bluntly dissected and retracted to expose the skull. A small cranial burr hole was drilled over the target cortical region using a microdrill, with careful preservation of the underlying dura mater. The animal was secured in a stereotaxic frame to stabilize head position and enable precise laser beam alignment.

A fiber-coupled orange laser (580 nm) was positioned above the exposed dural surface. The laser beam was collimated to a predefined spot diameter and delivered at constant power for continuous irradiation to trigger localized cortical oxidative stress and focal inflammatory injury. Laser power was calibrated with an optical power meter prior to each experiment to guarantee consistent radiant exposure across animals. During irradiation, the beam position was kept fixed to confine injury strictly within the targeted brain parenchyma.

After completion of laser exposure, the irradiation site was inspected for hemorrhage. The scalp and subcutaneous tissues were reapproximated and sutured in layers. Postoperative wound care was performed, and animals were returned to temperature-controlled housing for recovery.

Focal intra-abdominal organ injury modeling in rabbits

Three distinct intraperitoneal injury models, including pancreatic parenchymal injury, intestinal leakage, and gastric leakage, were sequentially established in New Zealand rabbits under sterile surgical conditions. Physiological parameters including heart rate, and respiratory rate, were continuously monitored throughout all procedures.

The ventral abdominal skin was depilated and disinfected with alternating povidone–iodine and 75% ethanol. A midline laparotomy was performed; subcutaneous and muscular layers were bluntly dissected to access the peritoneal cavity. The target visceral organs were gently exteriorized with moistened sterile gauze to avoid serosal desiccation.

For pancreatic injury modeling, the duodenal segment and adjacent pancreatic body were carefully isolated. A standardized partial-thickness parenchymal laceration was created on the pancreatic surface using a sharp microsurgical blade to induce localized pancreatic tissue damage and release of pancreatic digestive enzymes. Haemostasis was gently managed with cotton swabs without extensive electrocautery to preserve native inflammatory responses.

For intestinal leakage modeling, a full-thickness microperforation was generated on the antimesenteric wall of the proximal jejunum with a fine microsurgical needle. The perforation was left unrepaired to permit controlled leakage of intestinal contents into the peritoneal cavity. For gastric leakage, a small full-thickness defect was created on the gastric antrum wall, allowing slow extravasation of gastric fluid into the abdominal cavity. After each injury induction, the organs were returned to the peritoneal space.

After model creation, the abdominal wall fascia and cutaneous layers were closed in layers with sterile sutures. Postoperative analgesia and wound care were

administered. The flexible TWS sensor was deployed within the peritoneal cavity via the catheter-assisted implantation approach described above for continuous PH monitoring at the injury site.

In vivo implantation and locomotion characterization of the TWS

Minimally invasive in vivo implantation of the tiny wireless sensor (TWS) was implemented via customized surgical access strategies tailored to intracranial and abdominal anatomical microenvironments. For intracranial deployment, a microdrill was utilized to generate a cranial burr hole with a diameter marginally exceeding the 0.5 mm magnetic tip of the TWS. The distal sensing electrode was then stereotactically advanced through the dural layer into the intracranial cavity to complete intracranial positioning. Given the high compliance and deformability of the abdominal wall, a catheter-assisted minimally invasive implantation protocol was adopted for abdominal TWS delivery. A polyethylene catheter (outer diameter: 2.0 mm, inner diameter: 1.8 mm) was sleeved over a puncture needle and percutaneously inserted into the peritoneal cavity. Following steady cavity access establishment, the puncture needle was retracted, leaving the polyethylene catheter as a transient delivery channel. The TWS distal electrode was precisely navigated through the indwelling catheter into the abdominal cavity via magnetic guidance. After catheter removal, the TWS electrode was electrically interfaced with a wireless transceiver to finalize device assembly. For long-term in vivo implantation, the miniature wireless transceiver was implanted subcutaneously, which eliminates chronic percutaneous device penetration and substantially reduces the risk of postoperative infection and tissue inflammation.

Histological assessment of tissue injury after puncture and surgical implantation

To systematically evaluate local tissue trauma and inflammatory responses induced by two distinct abdominal implantation paradigms, a paired intra-animal

experimental design was adopted to eliminate individual biological variability. Prior to surgical manipulation, experimental rabbits were fully anesthetized via standard intravenous injection. The abdominal cutaneous hair was completely depilated, and the regional skin was sequentially disinfected with 75% ethanol and povidone-iodine solution to establish a sterile surgical field. For paired comparison, the left abdominal region of each rabbit was designated for conventional open surgical implantation, while the contralateral right abdominal region was assigned for minimally invasive puncture implantation, enabling direct side-by-side histological analysis of tissue damage induced by the two implantation strategies in the same individual animal.

For open surgical implantation, a 1–2 cm longitudinal mid-abdominal incision was precisely made on the preprocessed abdominal wall. The cutaneous and subcutaneous soft tissues were bluntly dissected to expose the peritoneal cavity, avoiding vascular and muscular damage. The functional device was gently deployed into the abdominal cavity at a fixed intraperitoneal position. After device placement, layered wound closure was performed: subcutaneous fascia and soft tissues were sequentially reapproximated, followed by continuous suture closure of the cutaneous layer with sterile surgical sutures to restore anatomical integrity. For minimally invasive puncture implantation, no surgical incision or suturing was required. The device was percutaneously delivered into the abdominal cavity through a customized minimally invasive puncture access channel. The puncture orifice was thoroughly disinfected post implantation to reduce superficial bacterial contamination risk.

All experimental animals were subjected to continuous postoperative health monitoring for 7 consecutive days, with daily assessment of wound healing status, activity level, and local tissue swelling. On postoperative day 7, all rabbits were humanely euthanized via intravenous administration of an overdose of pentobarbital

sodium. Peritoneal wall tissues surrounding both the surgical incision and puncture implantation sites were harvested en bloc, with a 3–5 mm marginal normal tissue reserved to cover the full range of local tissue response regions.

Collected tissue specimens were immediately fixed in 4% paraformaldehyde solution for 24 h at room temperature to stabilize tissue morphology. Subsequent histological processing was performed following standard paraffin embedding protocols: specimens were gradient dehydrated in serially concentrated ethanol solutions, cleared with xylene, and embedded in paraffin wax. Continuous tissue sections with a uniform thickness of 5 μm were prepared using a rotary microtome. For hematoxylin and eosin (H&E) staining, sections were deparaffinized in xylene and rehydrated through a descending ethanol gradient. Nuclei were stained with hematoxylin for 5–8 min, followed by differentiation in 1% hydrochloric acid-ethanol solution for moderate color separation. After rinsing with running distilled water for full color restoration, cytoplasmic and extracellular matrix components were counterstained with eosin for 1–3 min. Stained sections were further dehydrated via an ascending ethanol series, cleared with xylene, and permanently mounted with neutral balsam resin.

High-resolution histological imaging was acquired using an upright optical microscope under 4× low magnification and 20× high magnification objectives. Comparative histological analysis was performed to quantitatively and qualitatively evaluate differences in local tissue disruption, tissue structural integrity damage, inflammatory cell infiltration degree, and peripheral tissue edema between surgical implantation and minimally invasive puncture implantation groups.

Data availability

The authors declare that the main data supporting the findings of this study are available

within the article and its Supplementary Information files. Extra data are available from the corresponding author upon request.

Acknowledgments

This work was supported by Beijing Nova Program.

Author contributions

Z.L. and J.Z. conceived the idea and designed the research. Z.L., Y.Y. and Z.F. constructed the experimental platform. Z.L., Y.Y., and L.W. performed the research and analyzed the data. Z. L., Y. Y., and L. W. wrote the original draft. J. Z., N. L. and G. S. reviewed and edited the manuscript. Z. L., Y. Y. and L. W. created the visualizations. J. Z. supervised the project. J. Z. acquired the funding. Z. L., L. W. and Y.Y. contributed equally. All authors contributed to the discussion and wrote the manuscript.

Conflict of Interest

The authors declare no competing interests.

References

1. Chen, X. *et al.* pH sensing controls tissue inflammation by modulating cellular metabolism and endo-lysosomal function of immune cells. *Nat. Immunol.* **23**, 1063–1075 (2022).

2. Dhanik, A. *et al.* Root cause analysis of delayed emergency department computed tomography scans. *West. J. Emerg. Med.* **25**, 226–229 (2024).

3. Kucharzik, T. *et al.* ECCO-ESGAR-ESP-IBUS guideline on diagnostics and monitoring of patients with inflammatory bowel disease: part 1. *J. Crohn's Colitis* **19**, jjaf106 (2025).

4. Hu, J. *et al.* Bioresorbable acoustic patch for simultaneous sealing and early detection of gastric leakage. *Sci. Adv.* **12**, eaec6857 (2026).

5. *WHO Guidelines on Meningitis Diagnosis, Treatment and Care*.

http://www.ncbi.nlm.nih.gov/books/NBK614847/ (2025).

6. Madhvapathy, S. R. *et al.* Miniaturized implantable temperature sensors for the long-term monitoring of chronic intestinal inflammation. *Nat. Biomed. Eng.* **8**, 1040–1052 (2024).

7. Sonmezoglu, S., Fineman, J. R., Maltepe, E. & Maharbiz, M. M. Monitoring deep-tissue oxygenation with a millimeter-scale ultrasonic implant. *Nat. Biotechnol.* **39**, 855–864 (2021).

8. Mariello, M. *et al.* Wireless, battery-free, and real-time monitoring of water permeation across thin-film encapsulation. *Nat. Commun.* **15**, 7443 (2024).

9. Wang, B. *et al.* Next-generation biosensing for in situ monitoring. *Nat. Sens.* **1**, 111–130 (2026).

10. Tian, Y. *et al.* An implantable hydrogel-based phononic crystal for continuous and wireless monitoring of internal tissue strains. *Nat. Biomed. Eng* **9**, 1335–1348 (2025).

11. Wang, M., Jia, L., Jia, X., Li, H. & Feng, X. Flexible circuit-free system via passive modulated ultrasound for wireless thoracic pressure monitoring. *Sci. Adv.* **11**, eads5634 (2025).

12. Burton, A. *et al.* Wireless, battery-free subdermally implantable photometry systems for chronic recording of neural dynamics. *Proc. Natl. Acad. Sci.* **117**, 2835–2845 (2020).

13. Kim, J. *et al.* A wireless, implantable bioelectronic system for monitoring urinary bladder function following surgical recovery. *Proc. Natl. Acad. Sci.* **121**, e2400868121 (2024).

14. Li, S. *et al.* Bioresorbable, wireless, passive sensors for continuous pH measurements and early detection of gastric leakage. *Sci. Adv.* **10**, eadj0268 (2024).

15. Liu, J. *et al.* Bioresorbable shape-adaptive structures for ultrasonic monitoring of

deep-tissue homeostasis. *Science* **383**, 1096–1103 (2024).

16. Chen, J. C. *et al.* Endocisternal interfaces for minimally invasive neural stimulation and recording of the brain and spinal cord. *Nat. Biomed. Eng.* **9**, 896–904 (2025).

17. Xie, R. *et al.* A movable long-term implantable soft microfibre for dynamic bioelectronics. *Nature* **645**, 648–655 (2025).

18. Li, Z. *et al.* Self-sensing intelligent microrobots for noninvasive and wireless monitoring systems. *Microsyst. Nanoeng.* **9**, 102 (2023).

19. Gao, Q. *et al.* Soft magnetic microrobots with remote sensing and communication capabilities. *Nat. Commun.* **16**, 10489 (2025).

20. Hanson, L. C., Reinhardt, W. H., Shrager, S., Sivakumar, T. & Miskin, M. Z. Electrokinetic propulsion for electronically integrated microscopic robots. *Proc. Natl. Acad. Sci.* **122**, e2500526122 (2025).

21. Zhang, A. *et al.* Ultraflexible endovascular probes for brain recording through micrometer-scale vasculature. *Science* **381**, 306–312 (2023).

22. Luan, L. *et al.* Ultraflexible nanoelectronic probes form reliable, glial scar–free neural integration. *Sci Adv* **3**, e1601966 (2017).

23. Hu, C. *et al.* Bioresorbable electrochemical sensors for continuous deep-tissue lactate monitoring in critical care. *Nat. Commun.* https://doi.org/10.1038/s41467-026-74248-w (2026) doi:10.1038/s41467-026-74248-w.

24. Liu, T.-L. *et al.* Battery-free, tuning circuit–inspired wireless sensor systems for detection of multiple biomarkers in bodily fluids. *Sci. Adv.* **8**, eabo7049 (2022).

25. Ma, S. *et al.* Ultra-Sensitive and Stable Multiplexed Biosensors Array in Fully Printed and Integrated Platforms for Reliable Perspiration Analysis. *Adv. Mater.* **36**, 2311106 (2024).

26. Cortese, A. J. *et al.* Microscopic sensors using optical wireless integrated circuits.

Proceedings of the National Academy of Sciences **117**, 9173–9179 (2020).

27. Kim, M. *et al.* Wireless soft implantable pressure sensors based on liquid metal with large-area mapping and adaptive implantation capabilities. *Proc. Natl. Acad. Sci.* **123**, e2528796123 (2026).

28. Olenik, S. *et al.* A geometrically transient platform for bioelectronic implants. *Adv. Mater.* **38**, e73923 (2026).

29. Bae, J.-Y. *et al.* A biodegradable and self-deployable electronic tent electrode for brain cortex interfacing. *Nat. Electron.* **7**, 815–828 (2024).

30. Ho, J. S. *et al.* Wireless power transfer to deep-tissue microimplants. *Proc. Natl. Acad. Sci.* **111**, 7974–7979 (2014).

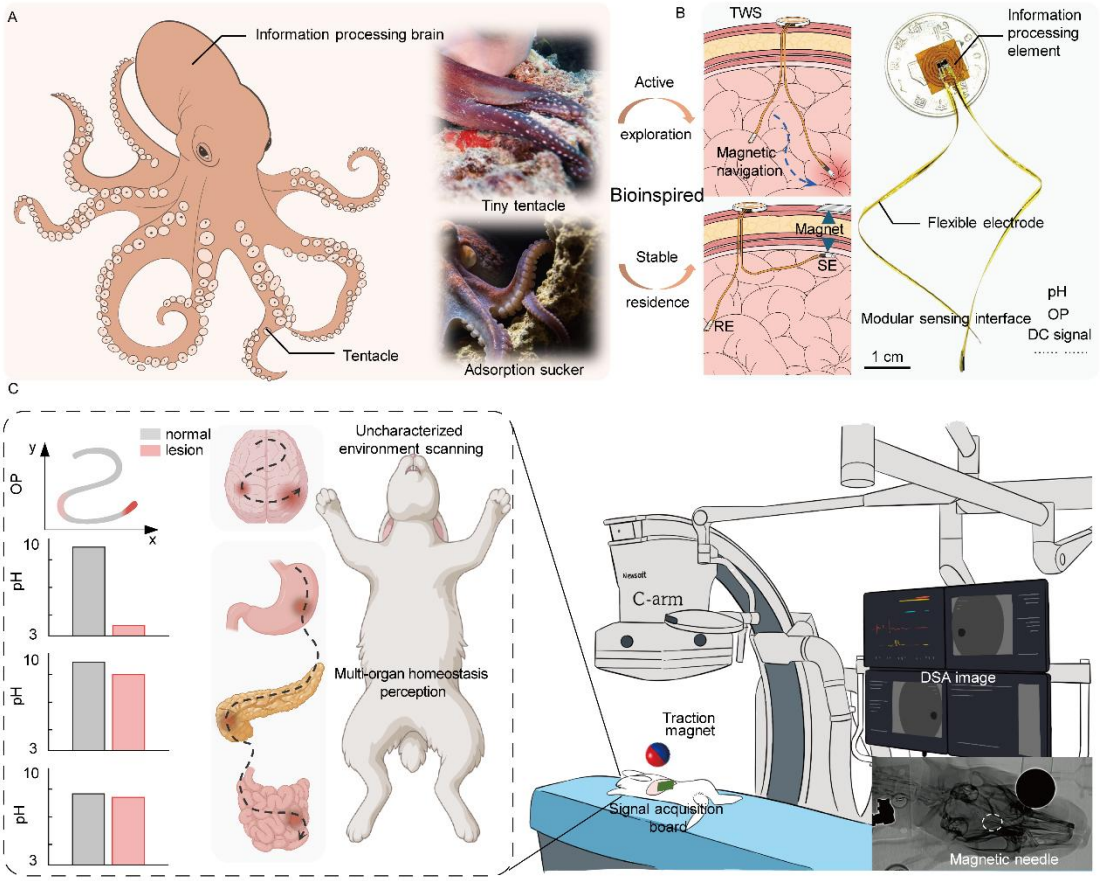


Figure 1. Concept of the octopus-inspired TWS for minimally invasive, spatially adaptive physiological sensing. (**A**) Conceptual inspiration from the octopus, which combines a central body for information processing with slender, highly dexterous tentacles that access confined rock crevices, explore the local environment and maintain stable contact through distal suckers. (**B**) Design of the tentacle wireless sensor (TWS). A relatively large wireless information-processing and readout unit remains extracorporeal or is implanted subcutaneously, whereas a thin and flexible tentacle-like sensing electrode is introduced through a small access opening for magnetically guided navigation, repositioning and fixation. A modular sensing interface at the distal tip converts local physiological parameters into voltage signals, enabling sensing modalities such as pH and

OP. (**C**) Working concept of the TWS. Under X-ray guidance, the mobile sensing interface actively scans previously uncharacterized anatomical regions or sequentially interrogate multiple organs, enabling spatially adaptive assessment of local physiological states.

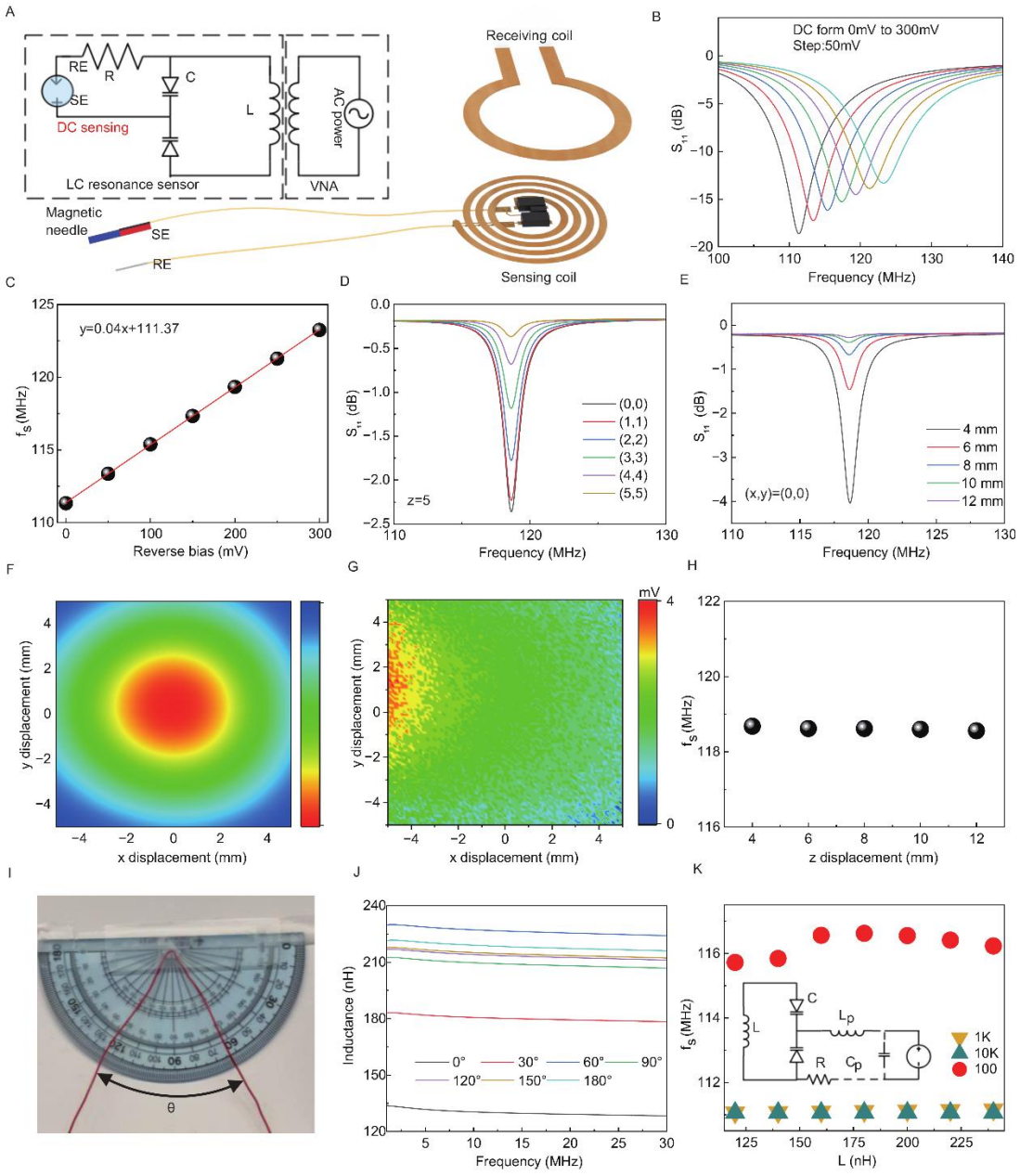


Figure 2. Working principle of TWS system. (**A**) Schematic of battery-free active environment exploration system (inset: Equivalent circuit of the sensing system). (**B**) Resonance curves of a sensor under DC reverse bias voltages from 0 to 300 mV, (step: 50 mV). (**C**) Measured resonant frequency (f_s) as a function of reverse bias voltage. (**D**) Resonance curves acquired at varying lateral distance. (**E**) Resonance curves acquired at

varying vertical distance. (**F** and **G**) Signal strength (**F**) and measurement precision (G) as a function of lateral distance from the origin (z = 5 mm). (**H**) Resonant frequency (f_s) as a function of the vertical distance (x = y = 0). (**I**-**K**) Influence of electrode motion angle on sensing. (**I**) Photograph of two electrode angles. (**J**) Inductance at different angles. (**K**) SPICE simulation of fs as a function of the parasitic inductance (L_p) and damping resistance (inset: equivalent circuit used for simulation; C_p=100 pF).

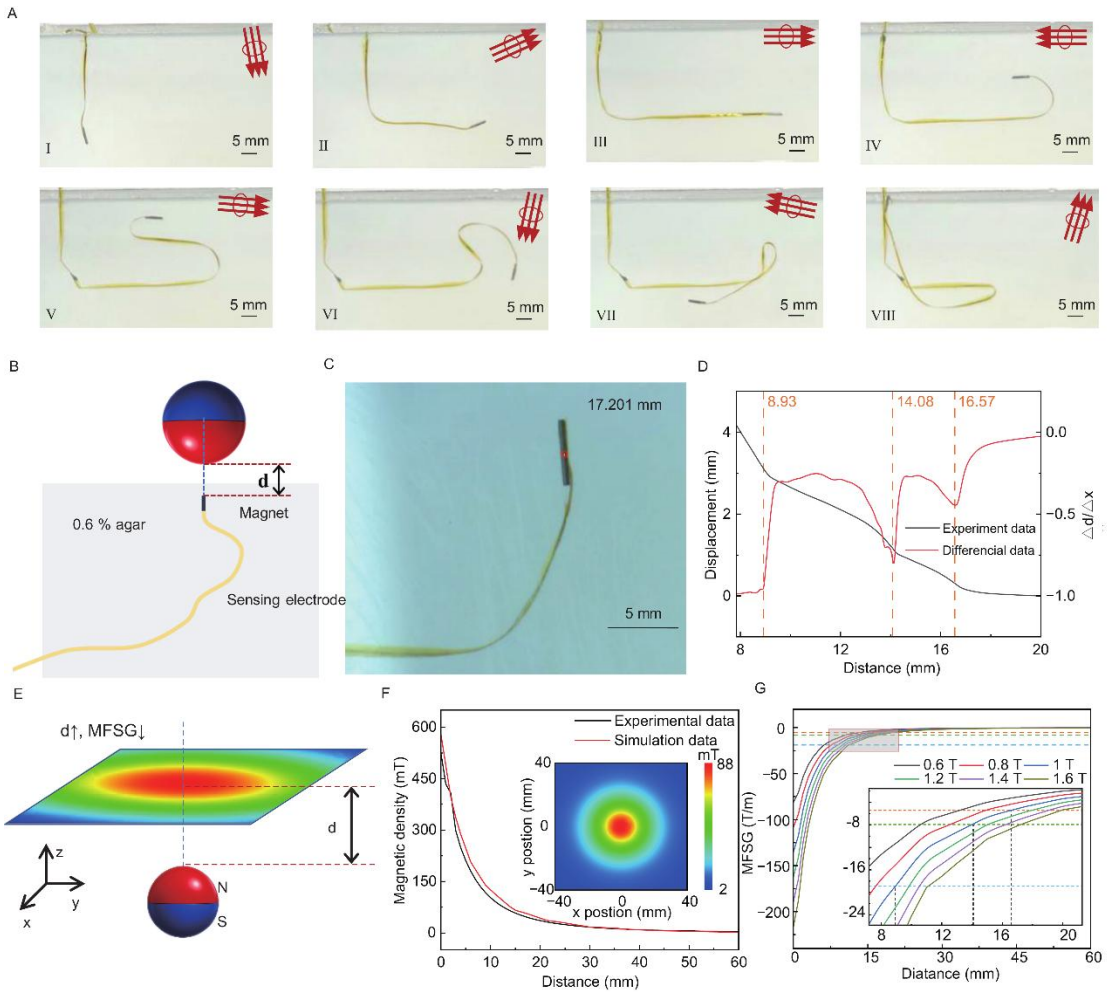


Figure 3. Navigation properties of TWS in an in vitro model. (**A**) Photographs of a single electrode scanning in agarose gel (0.6% wt) under magnetic navigation. The red arrow indicates the direction in which the TWS actively steers and navigates. TWS can exit through the entrance after scanning. (**B** and **C**) Schematic (**B**) and photograph (**C**) of the setup for detecting the driving force required by the electrode in agar by using magnetic balls (25 mm diameter). (**D**) Displacement of magnetic needle as a function of magnetic ball distance. The right axis is the differential of needle displacement with respect to distance. (**E**) Simulation of magnetic field strength of magnetic sphere. (**F**) Measured and simulated data of magnetic field intensity as a function of distance (inset: magnetic field

distribution at 10 mm). The residual magnetic field intensity of 0.8 T was used in the simulation. (**G**) Magnetic field strength gradient for different residual magnetic field intensity (horizontal line corresponds to the three MFSG values with rapid displacement of magnetic needle in (**D**)).

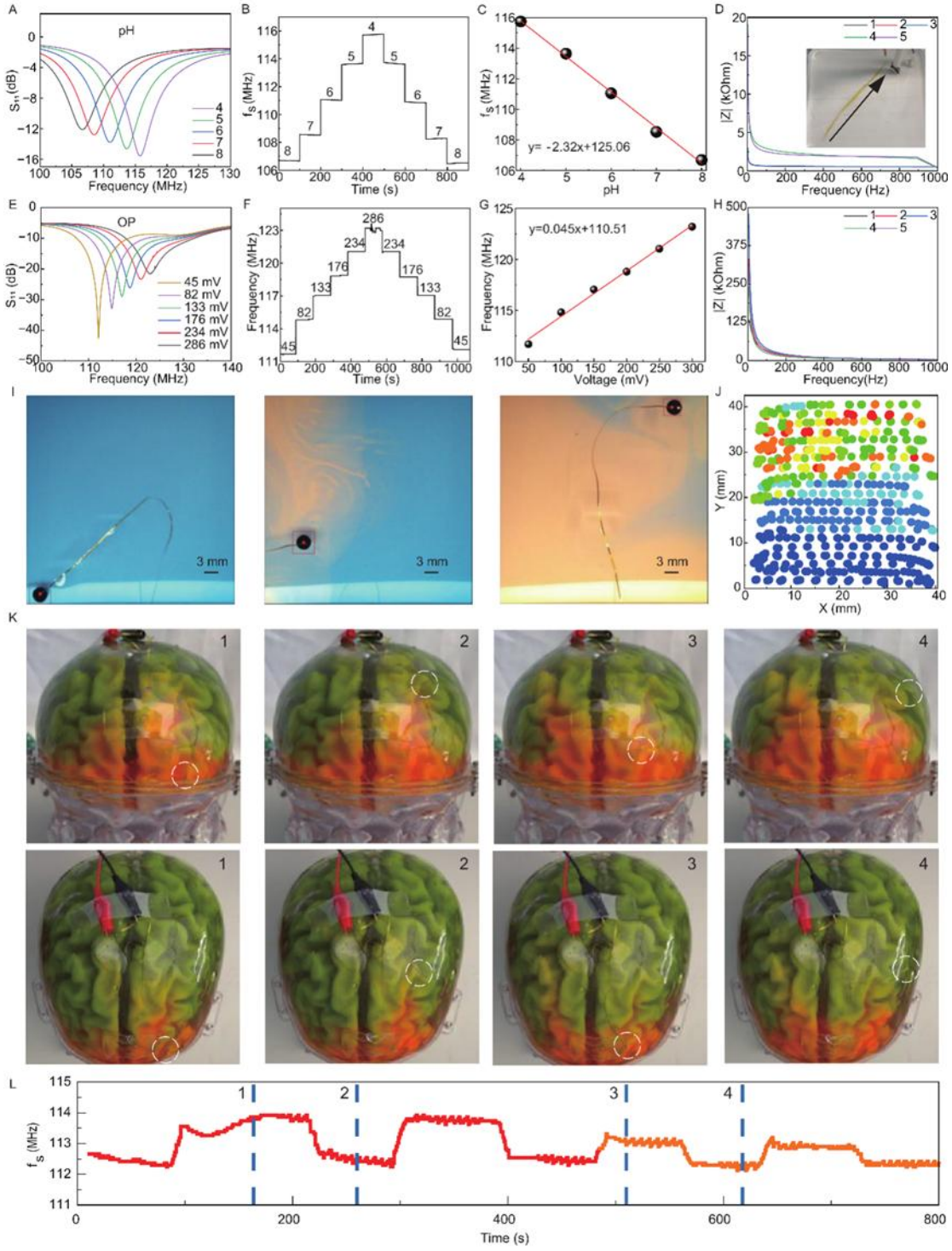


Figure 4. Physiological sensing and active patrolling performance of the TWS. (**A** and **E**) Response curves of functionalized TWS to pH (A) and oxidation potential (OP) (E). (**B**

and **F**) Cyclic step response of pH (B) and OP (F). (**C** and **G**) Resonant frequency f_s as a function of pH (C) and OP values (G). (**D** and **H**) Impedance of sensing electrodes at different distances in a 10 cm × 10 cm Petri dish with1 × PBS (**D**) and standard ORP solutions (86 mV) (**H**). (**I**) Two-dimensional mapping of the environment by the TWS (yellow means lower pH). (**J**) Spatial distribution of f_s during mapping in fig4. (I) (A color biased towards red means an increase in frequency). (**K** and **L**) Measurement photographs (**K**) and real-time results (**L**) of TWS in three-dimensional skull model, showing two reciprocating scans in the upper and lower pH regions.

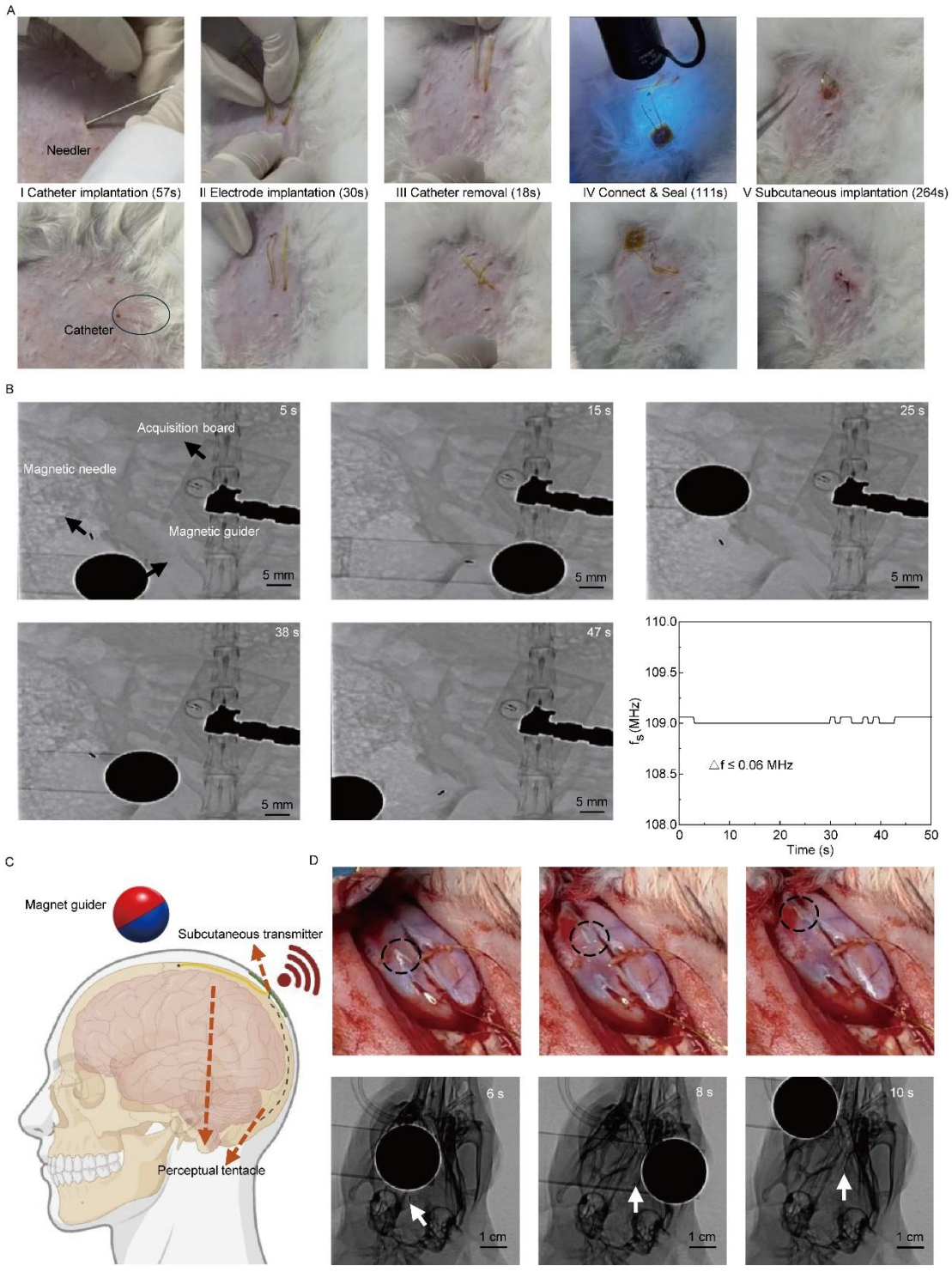


Figure 5. Minimally invasive implantation and in vivo active exploration of the TWS.

(**A**) Minimally invasive implantation of TWS through a puncture channel. The head coil is

implanted under the skin. (**B**) X-ray images and real-time results of TWS actively exploring in the abdominal cavity. The real-time results acquired during the process are shown in the last panel. (**C**) Schematic of the TWS performing magnetically guided, active intracranial steady-state analysis. (**D**) Motion characteristics of subdural TWS: photographs of TMC movement after skull removal (**top**) and X-ray images of TMC movement through a skull micropore (**bottom**).

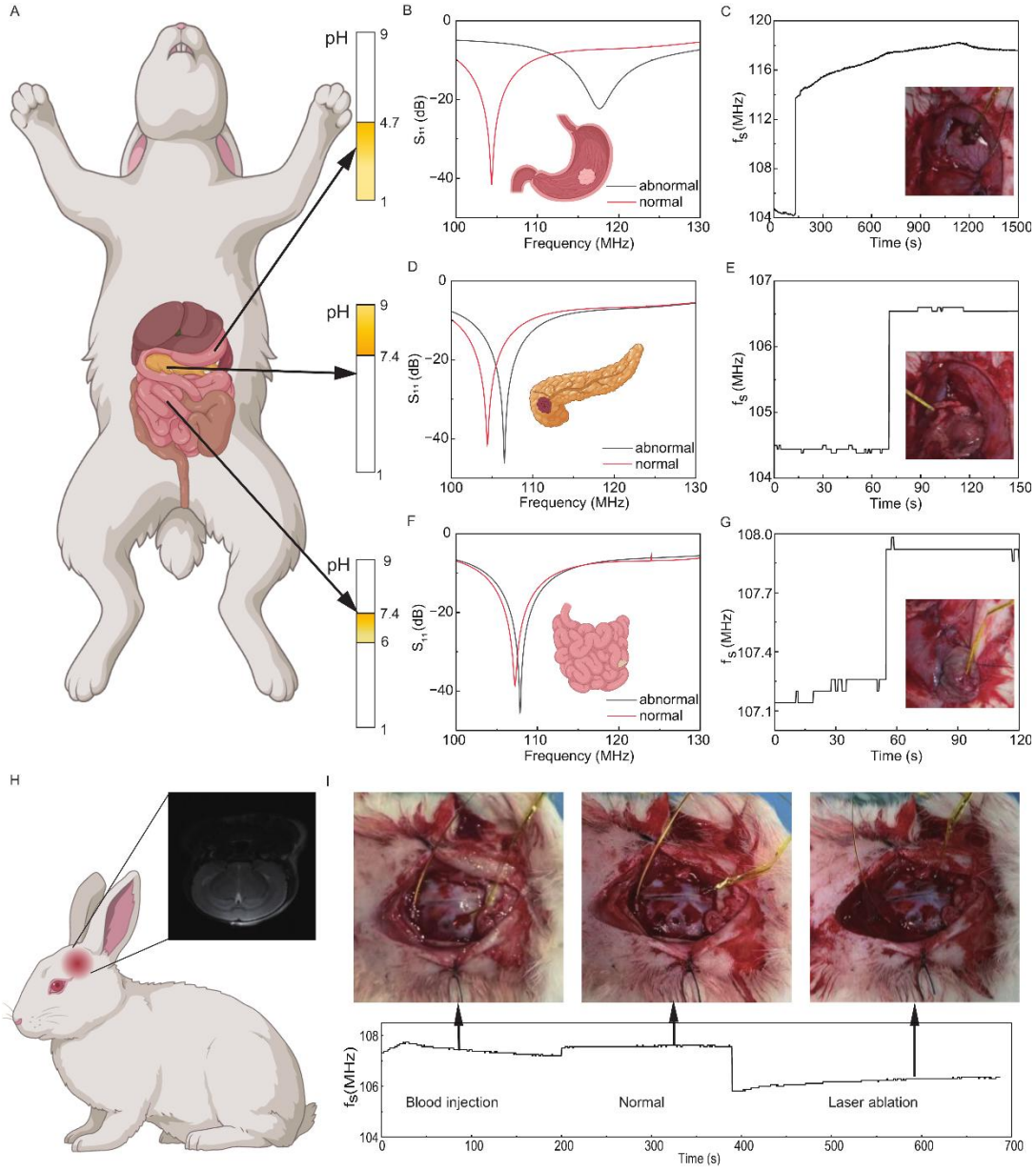


Figure 6. In vivo homeostasis monitoring with the TWS. (**A**) pH ranges of different organs in abdominal cavity. (**B** and **C**) Response curves (**B**) and real-time data (**C**) for normal and leaking stomach. (**D** and **E**) Response curves (**D**) and real-time data (**E**) of normal and damaged pancreas. (**F** and **G**) Response curves (**F**) and real-time data (**G**) of normal and leaking small intestine (**H**) Monitoring of intracranial inflammation in rabbits

(inset: MRI image of rabbit head used for verification). (**I**) TWS evaluation of different intracranial inflammation models: Photographs of three different areas: blood injection, normal area and laser photothrombotic injury (**top**) and real-time oxidation potential measurements (**bottom**). The TWS remained stable in each region for a period of time.